

## RESEARCH ARTICLE

[View Article Online](#)  
[View Journal](#)

Cite this: DOI: 10.1039/d0qi00921k

# Theoretical study of Na<sup>+</sup> transport in the solid-state electrolyte Na<sub>3</sub>OBr based on deep potential molecular dynamics†

Han-Xiao Li, Xu-Yuan Zhou, Yue-Chao Wang and Hong Jiang \*

Recent discoveries in the antiperovskite-class sodium superionic conductors call for a thorough molecular dynamics (MD) study of sodium ion mobility, but the practical use of MD is often hindered by the accuracy-vs.-efficiency dilemma. Here we applied the recently developed deep potential molecular dynamics (DeePMD) approach to investigate the ion mobility in Na<sub>3</sub>OBr. With the deep potential model for Na<sub>3</sub>OBr constructed based on first-principles density-functional theory (DFT) calculations, we directly calculate the Na<sup>+</sup> diffusion coefficient at various temperatures, and obtain an activation energy of 0.42–0.43 eV. This in comparison with the 0 K migration barrier (0.41–0.43 eV) suggests that the finite temperature effect is negligible for Na<sub>3</sub>OBr. The model gives an extrapolated room temperature ionic conductivity of  $1 \times 10^{-4}$ – $2 \times 10^{-4}$  mS cm<sup>-1</sup>, roughly in the same order of magnitude as the experimental results. We also confirm the proportionality of the diffusion coefficient with respect to the vacancy concentration, and find that the migration barrier is relatively insensitive to the vacancy concentration. This work further demonstrates the promising role of the DeePMD method in the study of the transport properties of solid-state electrolytes.

Received 30th July 2020,  
Accepted 1st November 2020  
DOI: 10.1039/d0qi00921k  
[rsc.li/frontiers-inorganic](http://rsc.li/frontiers-inorganic)

## 1. Introduction

The rapid development of the economy and society has put forward an increasing demand for large-scale energy storage devices. All-solid-state sodium-ion batteries are promising candidates due to their enhanced safety and the abundance of raw materials.<sup>1,2</sup> Sodium superionic conductors are key to developing such batteries.<sup>3,4</sup> Although a lot of effort has been made in this area, currently there are only a few sodium superionic conductors that can reach a conductivity comparable to traditional organic electrolytes ( $\sim 1$  mS cm<sup>-1</sup>). These include Na<sub>3</sub>PSe<sub>4</sub>,<sup>5</sup> Na<sub>3</sub>Zr<sub>2</sub>Si<sub>2</sub>PO<sub>12</sub> (NASICON),<sup>6</sup> Na-β"-Al<sub>2</sub>O<sub>3</sub>,<sup>7</sup> etc.

Sodium-rich antiperovskites, represented by Na<sub>3</sub>OBr, were inspired from their lithium counterpart, Li<sub>3</sub>OCl. The latter was found to be superionic in 2012, with an ionic conductivity of  $\sim 1$  mS cm<sup>-1</sup> at room temperature (RT).<sup>8</sup> Although Na<sub>3</sub>OBr only exhibited an RT ionic conductivity of  $10^{-5}$ – $10^{-4}$  mS cm<sup>-1</sup>,<sup>9</sup> theoretical and experimental research showed that its conductivity can be significantly enhanced *via* structural and chemical manipulation approaches.<sup>10,11</sup> In a recent study<sup>12</sup> that we

participated in, a newly synthesized compound Na<sub>3</sub>OBH<sub>4</sub> was even found to possess an RT conductivity of 4.4 mS cm<sup>-1</sup>—the highest among all the currently known sodium-rich antiperovskites. Our calculation based on density-functional theory (DFT) showed that the 0 K sodium-ion migration barrier in Na<sub>3</sub>OBH<sub>4</sub> was lower than that of Na<sub>3</sub>OBr by about 0.1 eV; however, this cannot account for the difference in conductivity quantitatively, which necessitated the direct molecular dynamics (MD) simulation of the ionic conductivity.

Currently there are two major classes of molecular dynamics simulations: *ab initio* molecular dynamics (AIMD) and force-field based molecular dynamics. The former has the accuracy of density functional theory (DFT), but its high computation cost greatly limits the size of the system under study and the duration of simulation, and thus it cannot give enough migration counts to enable the direct calculation of the ionic conductivity. The latter possesses superiority in the time and length scales, but the reliability of force-fields is often questionable, especially for chemical and physical processes involved in inorganic materials like Na<sub>3</sub>OBr and Na<sub>3</sub>OBH<sub>4</sub>. Recent developments of machine-learning (ML) interatomic potential methods bring hope toward addressing this dilemma.<sup>13–15</sup> A number of ML-based approaches have been developed to train force-fields with first-principles data, thus combining the efficiency of force-fields with the accuracy of first-principles electronic structure theory.<sup>14,15</sup> The recently

Beijing National Laboratory of Molecular Science, College of Chemistry and Molecular Engineering, Peking University, Beijing 100871, China.  
E-mail: [jianghchem@pku.edu.cn](mailto:jianghchem@pku.edu.cn)

†In celebration of the 110th anniversary of the College of Chemistry and Molecular Engineering of Peking University.

proposed deep potential molecular dynamics (DeePMD)<sup>16–18</sup> method based on a deep neural network representation of inter-atomic potentials is particularly attractive by virtue of its highly automatic active learning procedure and uniformly accurate description of the potential energy surface.<sup>18</sup>

There are already a few theoretical studies of ion diffusion in solid state electrolytes by ML-based approaches.<sup>19–22</sup> Li *et al.*<sup>20</sup> investigated lithium ion diffusion in amorphous Li<sub>3</sub>PO<sub>4</sub> using the neural network (NN) ML potential method developed by Behler and coworkers,<sup>13</sup> and they found that the NN potential can well reproduce DFT results with the root residual mean square errors of about 0.6 meV per atom for the test set, and the calculated diffusion barriers from DFT and the NN potential agreed well with differences of less than 0.05 eV. Marcolongo *et al.*<sup>22</sup> assessed the performances of the DeePMD approach to model ion diffusion by considering three well-known solid state electrolytes Li<sub>10</sub>GeP<sub>2</sub>S<sub>12</sub>, Li<sub>7</sub>La<sub>3</sub>Zr<sub>2</sub>O<sub>12</sub> and NASICON, and found good agreement with the experiment or previous computational studies. Using a different implementation of the ML potential,<sup>19</sup> Miwa and coworkers studied Li ion transport in Li<sub>2</sub>B<sub>12</sub>H<sub>12</sub><sup>19</sup> and Li<sub>7–x</sub>La<sub>3</sub>(Zr<sub>2–x</sub>Nb<sub>x</sub>)O<sub>12</sub>,<sup>21</sup> also with remarkable accuracy. In this work, we further explore the applicability of the DeePMD approach in antiperovskite-type materials. We take Na<sub>3</sub>OBr as an example to construct the deep potential (DP) force field based on DFT calculations, and use it to study the transport properties of Na ions at a finite temperature. The paper is organized as follows: in section 2, we introduce the basics of DeePMD and other theoretical methods used in this study and present important computational details. In section 3, we assess the performance of our DP model and use it to calculate the transport properties of Na<sub>3</sub>OBr, including the ionic conductivity and activation energy. We will also investigate the effect of vacancy on Na<sup>+</sup> transport. In section 4, we summarize the main findings of this study and present an outlook of future work.

## 2. Theoretical methods and computational details

### 2.1 Construction of the DP force field

We use the DeepPot-SE<sup>17</sup> force-field as implemented in the DeePMD-kit.<sup>23</sup> In this approach, the total energy of a system is expressed as a sum of “atomic” energies each depending on the local environment of the corresponding atom:

$$E = \sum_i E_i \quad (1)$$

The “atomic” energy  $E_i$  is obtained in the following steps: first, a neighbor list is set up for atom  $i$  that includes all its neighbors within a cutoff radius  $r_c$ . The radial and angular information of these atoms’ position relative to atom  $i$  is stored in a generalized local environment matrix. To eliminate the discontinuity caused by truncation, the matrix elements have been multiplied by a weighting function which decays smoothly from unity to zero when the interatomic distance

increases from a smooth cutoff parameter  $r_{sc}$  to the cutoff radius  $r_c$ . The generalized local environment matrix is then mapped onto the descriptors that preserve the translational, rotational and permutational symmetry through a local embedding network. Finally, the descriptors of all the atoms are fed into a neural network and subjected to a series of linear and nonlinear transformations to give  $E_i$ . In the case of Na<sub>3</sub>OBr, we set  $r_c$  to 6.0 Å and  $r_{sc}$  to 5.8 Å, which are large enough to include Na ions in the second coordination shell.

The construction of a DP force-field requires a relatively large amount of training data, which is obtained using the Vienna *Ab initio* Simulation Package (VASP).<sup>24</sup> Projector augmented wave<sup>25</sup> pseudopotentials are used to treat core–valence interactions, and the electronic exchange–correlation is treated with the PBEsol functional<sup>26</sup> to achieve a better description of the equilibrium lattice properties.<sup>27,28</sup> For computational tractability, the cutoff energy for the planewave expansion is set to 300 eV and a gamma-only  $k$ -mesh is used for all supercell calculations.

In order to generate the training set more efficiently, we use the DP-GEN code<sup>29</sup> to carry out concurrent learning.<sup>18</sup> The basic idea of concurrent learning is to gradually improve the sampling of the potential energy surface (PES) through training–exploration–labeling iterations. To begin with, a short-time AIMD simulation is performed to generate the initial training set and four DP force-fields are trained with different network initialization parameters. Then one of the four force-fields is used to explore the PES through MD simulations. The snapshots obtained in this process are evaluated with the four DP force-fields to give the force on each atom. The structures that show a large model deviation (*i.e.* the differences between the forces predicted by the four force fields are larger than a certain criterion) are labeled for *ab initio* calculations, and are added to the training set of the next iteration. Since sampling the whole PES can be time consuming, in some circumstances, it is more convenient to limit the exploration space to a certain region of the PES. Therefore, we trained two types of force-fields to meet different requirements of practical use, namely, the DP-F and DP-G force fields.

**2.1.1 DP-F (F stands for fixed).** This type of force-field trades generality for simplicity, as it is intended for a single lattice parameter and vacancy concentration. Such a force-field is relatively easy to train, and may still find use in calculating the Na<sup>+</sup> migration barrier and ionic conductivity under the desired conditions. In our case, we constructed a  $2 \times 2 \times 2$  supercell with the experimental lattice parameter at 300 K ( $a = 4.57$  Å) and introduced a Na vacancy manually. The MD simulations in the exploration stage were carried out at 1000 K in the NVT ensemble, and *ab initio* calculations were performed for snapshots with a model deviation larger than  $0.04 \text{ eV Å}^{-1}$ . Throughout all the iterations, the lattice parameter and vacancy concentration were kept unchanged.

**2.1.2 DP-G (G stands for general).** In contrast to DP-F, this type of force-field is designed to work for variable-cell simulations with different vacancy concentrations. For simplicity, we denote  $m_1 \times m_2 \times m_3$  supercells with  $n$  vacancies as  $m_1 m_2 m_3 v n$ . To train such a force-field, we include 222v0 and

222v1 configurations in the training set and explore a temperature range of 700 K–1300 K. As the iteration progresses, we gradually scale the starting configurations in the exploration stage to make the force-field adapt to different lattice parameters. The scaling factors are limited to no more than  $\pm 2\%$ .

## 2.2 MD simulations

MD simulations are used to obtain the equilibrium lattice parameters and diffusive properties of  $\text{Na}_3\text{OBr}$ . This work involves AIMD and DP force-field based MD, denoted as DPMD henceforth, performed with VASP and the Large-scale Atomic/Molecular Massively Parallel Simulator (LAMMPS),<sup>30</sup> respectively.

Equilibrium lattice parameters at finite temperatures are determined by MD simulations in the NPT ensemble ( $P = 1$  bar). All simulations are performed on a stoichiometric  $2 \times 2 \times 2$  supercell, with a time step of 2 fs. After an equilibration time of 5 ps, 27 consecutive MD runs each lasting 2 ps are carried out to determine the equilibrium cell volume and to estimate its uncertainty. The equilibrium lattice parameter and its uncertainty are calculated accordingly, assuming that the simulation cell is cubic. In AIMD simulations, the cutoff energy is increased to 600 eV to minimize the effect of the Pullay stress.<sup>31</sup>

The diffusive properties are calculated with MD simulations in the NVT ensemble with the simulation cells built using the experimental lattice parameter at 300 K ( $a = 4.57$  Å), a practice commonly used in the literature.<sup>10,32,33</sup> To speed up the migration of Na ions, Na vacancies are created and the simulations are performed at elevated temperatures (700–1300 K). For the evaluation of the diffusion coefficient ( $D$ ) and its uncertainty at a certain temperature, a long-time simulation is performed with a time step of 2 fs, and is subsequently cut into several slices (see sections 3.2 and 3.3 for details) for statistical analysis. The diffusion coefficient of each slice is obtained from the Einstein–Smoluchowski relation<sup>34</sup>

$$\frac{\partial \langle \Delta r^2(t) \rangle}{\partial t} = 6D \quad (2)$$

where  $\langle \Delta r^2(t) \rangle$  is the mean square displacement (MSD) averaged over all Na ions and time origins. In practice, we select 100 time origins evenly spread over the period of the slice, and calculate the MSD as

$$\langle \Delta r^2(t) \rangle = \frac{1}{N_s N_a} \sum_k \sum_i^{N_a} |\mathbf{r}_i(t_k + t) - \mathbf{r}_i(t_k)|^2 \quad (3)$$

where  $\mathbf{r}_i(t)$  is the position vector of the  $i$ -th Na ion at time  $t$ ,  $N_a$  is the number of Na ions in the simulation cell,  $t_k$  is the  $k$ -th time origin, and  $N_s = 100$  is the total number of time origins. The diffusion coefficient is then obtained by fitting the linear regime of the MSD- $t$  profile to eqn (2). Finally, the diffusion coefficients calculated from all slices are averaged to obtain the diffusion coefficient of the corresponding temperature, and their standard deviation is taken as the uncertainty. The

apparent activation energy  $E_a$  is obtained from an Arrhenius fit of the diffusion coefficient with respect to the temperature:

$$\lg D = -\frac{E_a}{2.303k_B T} + A \quad (4)$$

and an extrapolation is performed to give the RT diffusion coefficient. The ionic conductivity is further calculated according to the Nernst–Einstein relation<sup>34</sup>

$$\sigma = \frac{Nq^2 D}{Vk_B T} \quad (5)$$

where  $N$  is the number of Na ions,  $q$  is the elementary charge, and  $V$  is the volume of the simulation cell.

## 2.3 NEB calculations

The 0 K Na<sup>+</sup> migration barriers are calculated using the climbing image nudged elastic band method<sup>35,36</sup> (CI-NEB, shortened as NEB hereafter) as implemented in the VASP-vtst toolkit<sup>37</sup> and the Python ASE module.<sup>38</sup> Supercells are constructed with the experimental lattice parameter at 300 K ( $a = 4.57$  Å), and Na vacancies are introduced manually. During the optimization, the shape and volume of the supercells are fixed, while the internal degrees of freedom are allowed to relax. The force convergence criterion is set to 5 meV Å<sup>-1</sup>.

# 3. Results and discussion

## 3.1 Performance of DP-F and DP-G force fields

The DP-F force-field is obtained after 8 iterations of concurrent learning, and the final training set contains 4628 222v1 configurations. DP-G takes longer (18 iterations), and the final training set consists of 2498 222v0 configurations and 3125 222v1 configurations. To examine the accuracy of the two force-fields, we randomly select 300 configurations (not included in the training set) on each kind of supercell as testing sets, and evaluate the root mean square error (RMSE) of the energy and force. The results are presented in Table 1. We notice that DP-F is more accurate than DP-G for the testing set of 222v1 with the same lattice constant as that used in the training set. But for testing sets that contain configurations with different lattice constants and/or vacancy concentrations, DP-G is much more accurate than DP-F. As clearly shown in Fig. 1, DP-G is highly accurate in reproducing DFT energies

**Table 1** Root mean square error (RMSE) of the energy and force on different testing sets. 222v1 is short for “2 × 2 × 2 supercell with one vacancy”; the same rule applies to 223v1 and 222v0. The numbers in parentheses are the results of DP-F for a testing set with the same lattice constant as that used in the training set

	Energy (meV per atom)			Force (meV Å <sup>-1</sup> )		
FF	222v1	223v1	222v0	222v1	223v1	222v0
DP-F	20.4 (0.6)	32.5	55.8	21.4 (13.4)	13.0	22.8
DP-G	2.3	2.4	1.1	18.8	16.7	10.5

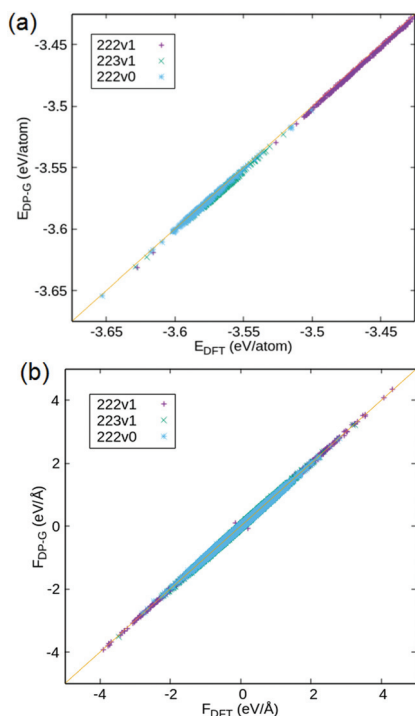


**Fig. 1** Comparison of the (a) energy and (b) force given by DP-G and DFT on three testing sets. 222v1, 223v1 and 222v0 refer to the vacancy concentration of the testing sets (see the caption of Table 1).

and forces, and its force prediction error is quite low compared to those developed for other extended systems in the original DeepPot-SE paper.<sup>17</sup> It is also important to note that the training of DP-G only involves  $2 \times 2 \times 2$  supercells, and the lowest nonzero vacancy concentration available is about 4% (222v1). Although the actual vacancy concentrations in experiments are still lower ( $\sim 1\%$ ),<sup>9</sup> we do not include them in the training set since they require larger supercells and greatly increase the computational cost. Instead, we use 300 223v1 configurations to test the transferability of DP-G with respect to the vacancy concentration. Care should be taken in this process, for the  $k$ -point density of  $2 \times 2 \times 3$  supercells does not match that of the  $2 \times 2 \times 2$  supercells, and a systematic numerical error exists in the DFT total energies. After compensating for this energy shift, the energy prediction error of DP-G on the 223v1 testing set is 2.4 meV per atom—not much larger than that for 222v1. This suggests that the DP-G force-field trained with 222v0 and 222v1 configurations is applicable to the systems with intermediate vacancy concentrations.

As a second test of the force-fields, we use them to perform NEB calculations to obtain the Na migration barrier in a 222v1 supercell. For comparison, we also perform the same calculation with DFT. The migration barriers obtained with DP-F and DP-G are 0.41 eV and 0.43 eV respectively, compared to the DFT result of 0.41 eV. This illustrates again that DP-F can be extremely accurate for structures sharing the same lattice parameter as its training set. The error of DP-G is slightly larger but still acceptable for NEB calculations.

**Table 2** Equilibrium lattice parameters ( $a$ , in angstrom) of  $\text{Na}_3\text{OBr}$  at various temperatures given by DP-F, DP-G, and DFT. 0 K lattice parameters are obtained from equation-of-state scanning on a unit cell; finite-temperature parameters are obtained from MD simulations in the NPT ensemble on a  $2 \times 2 \times 2$  supercell, and the uncertainties are shown in parentheses. Experimental lattice parameters are from ref. 9

$T/\text{K}$	DP-F	DP-G	DFT	Expt
0	4.589	4.519	4.507 <sup>a</sup>	—
300	4.637(3)	4.555(3)	4.567(1)	4.567
400	4.654(4)	4.571(4)	4.581(2)	4.577
500	4.669(7)	4.590(5)	4.597(4)	4.586
700	4.709(8)	4.626(8)	4.628(4)	—
800	4.727(9)	4.647(9)	4.646(4)	—
900	4.75(1)	4.665(9)	4.665(6)	—
1100	Crashed	4.71(1)	4.705(8)	—
1300	—	4.77(2)	4.75(2)	—

<sup>a</sup> To be consistent with the DFT results at finite temperatures, this calculation uses a  $2 \times 2 \times 2$   $k$ -mesh and a cutoff energy of 600 eV.

To further test the performance of the force-fields in practical use, we perform equation-of-state scanning and MD simulations in the NPT ensemble to determine the equilibrium lattice parameters of  $\text{Na}_3\text{OBr}$  at various temperatures. These tests serve as an indicator whether the force-fields work for different lattice parameters. As can be seen in Table 2, DP-G agrees well with DFT in the whole temperature range and reproduces the experimental lattice parameters whenever the latter are available. In contrast, DP-F significantly overestimates the equilibrium lattice parameters. It even predicts the system to crash at 1100 K, a temperature at which the system should be stable according to the AIMD results. This clearly indicates that DP-F gives unreasonable forces when there is a change in the lattice parameter, demonstrating the necessity to use DP-G force fields in this situation.

### 3.2 Application to long-time MD simulations

The original purpose of using DeepMD on  $\text{Na}_3\text{OBr}$  is to calculate its ionic conductivity. In previous AIMD simulations, the simulation time was extremely limited ( $\sim 100$  ps), and the number of successful  $\text{Na}^+$  migrations was less than 10 even at a temperature of 900 K.<sup>12</sup> This made the direct calculation of the ionic conductivity almost impossible, since a minor difference in the migration count may have a huge impact on the result. The insufficiency in sampling greatly affected the shape of the MSD- $t$  profile and made it difficult to apply the Einstein-Smoluchowski relation (Fig. 2(a)). Now that the DP force-fields are available, we make full use of its time-scale advantage and increase the simulation time to 5 ns. As shown in Fig. 2(b), the MSD- $t$  profile already shows a linear characteristic, suggesting that a slice length of 5 ns is sufficiently long.

To obtain the RT ionic conductivity, we calculate the diffusion coefficients at 700, 800, 900, 1000, 1100 and 1300 K to perform the Arrhenius fit. Following the common practice as in ref.10, 32 and 33, we carry out the simulations on a 222v1 supercell and use the same lattice parameter for all temperatures. For error estimation, we perform a simulation of 30 ns



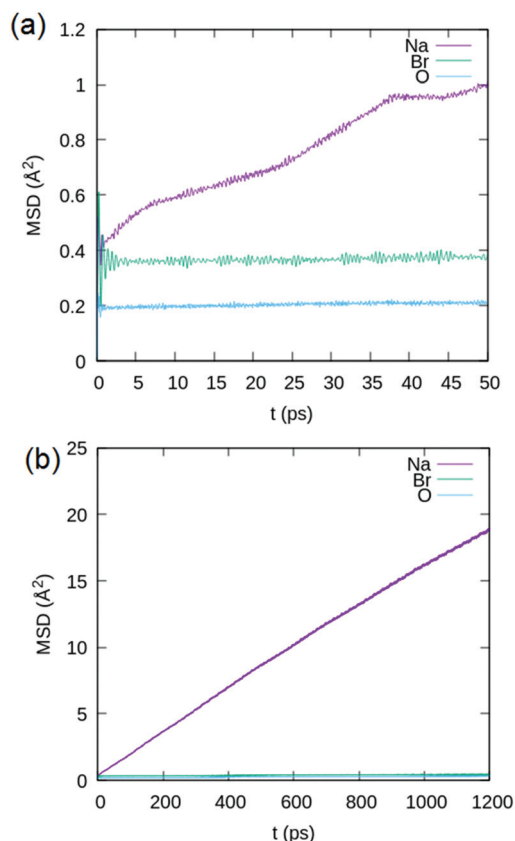


**Fig. 2** Illustration of MSD vs. time ( $t$ ) calculated according to eqn (3) from MD simulations at 900 K. (a) AIMD lasting 100 ps and (b) DPMD lasting 5 ns, using the DP-F force-field.

for each temperature and cut it into 6 slices. The results obtained with DP-F and DP-G are shown in Fig. 3. These results show the Arrhenius behavior well, and the error bars are quite small (generally no greater than 0.1 in  $\lg D$ ). The extrapolated RT ionic conductivities given by DP-F and DP-G are  $9 \times 10^{-4} \text{ mS cm}^{-1}$  and  $6 \times 10^{-4} \text{ mS cm}^{-1}$ , respectively. Note that the vacancy concentration in our simulations is 4%—about four times higher than that observed in experiments. Assuming the proportionality of the ionic conductivity with respect to the vacancy concentration (see the results in section 3.3), the calculated RT ionic conductivity corresponding to the experimental  $\text{Na}^+$  vacancy concentration should be  $1 \times 10^{-4}$ – $2 \times 10^{-4} \text{ mS cm}^{-1}$ , which is roughly in the same order of magnitude as the experimental results.<sup>9</sup>

Another key property obtained from the Arrhenius fit is the apparent activation energy. With the lattice parameter and vacancy concentration fixed, this is just the  $\text{Na}^+$  migration barrier at a finite temperature. DP-F and DP-G give apparent activation energies of 0.42 eV and 0.43 eV, respectively—almost identical to the NEB migration barriers at 0 K. Intuitively, one may think that the activation energy at a finite temperature should be higher than the NEB barrier as a result of the irregular scattering of Na ions by their surroundings. However, this finite temperature effect is apparently rather weak for  $\text{Na}_3\text{OBr}$ ,

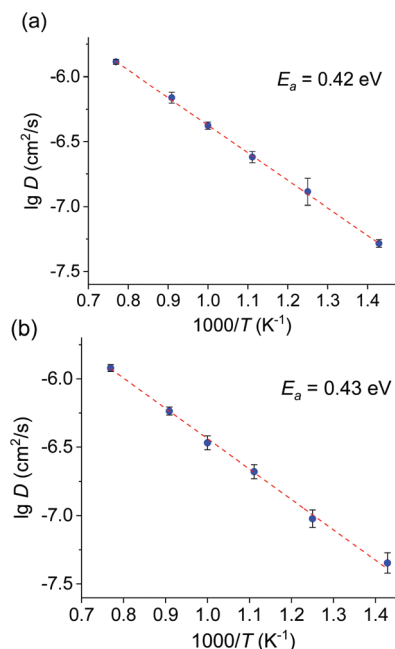


**Fig. 3** Arrhenius fit of the diffusion coefficient as a function of the temperature in  $\text{Na}_3\text{OBr}$  calculated with (a) DP-F and (b) DP-G. The error bars are estimated from 6 slices each lasting 5 ns.

and the NEB barrier can be regarded as a very good approximation of the finite-temperature migration activation energy. We note that our calculated barriers are larger than those from previous studies (0.32–0.35 eV),<sup>10,11</sup> which is possibly due to the different choice of density-functional approximations, pseudopotentials, and other *ab initio* calculation settings, rather than the DP model itself. Finally, we should point out that our results are not directly comparable to the apparent activation energy measured in experiments ( $\sim 0.7 \text{ eV}$ ),<sup>9,11</sup> for the latter may involve more complicated factors that are not considered in our simulations. First of all, the thermal expansion of the crystal lattice may further increase the diffusion coefficient at elevated temperatures, resulting in a steeper Arrhenius plot and thus a higher apparent activation energy. Secondly, the vacancy concentration may also vary with the temperature under experimental conditions, and the measured apparent activation energy actually includes the contribution of vacancy formation.<sup>34</sup> Last but not least, the sample prepared in experiments may contain dislocation, grain boundaries and other defects,<sup>8,11</sup> which may hinder the transport of Na ions and give rise to a higher activation energy.<sup>39</sup>

### 3.3 Effects of the vacancy concentration on $\text{Na}^+$ migration

The efficiency of DeePMD also enables calculations on larger supercells, with which we can systematically study the influence of the vacancy concentration on  $\text{Na}^+$  migration. To start with, we focus on the convergence of the  $\text{Na}^+$  migration barrier with respect to the supercell size. Previous *ab initio* studies on antiperovskites<sup>10,32</sup> usually performed NEB calculations on 222v1 supercells due to the limitation of computation

**Table 3** Na<sup>+</sup> migration barriers in various supercells, given by NEB calculations with DP-F and DP-G force-fields

Supercell	Migration barrier (eV)	
	DP-F	DP-G
221v1	0.45	0.46
222v1	0.41	0.43
331v1	0.40	0.41
332v1	0.41	0.42
333v1	0.41	0.42
444v1	0.42	0.43

resources; however, the corresponding vacancy concentration was significantly higher than that under typical experimental conditions, and therefore it could be questionable whether the results reflected the real migration barrier. With the DP force-fields, we carry out NEB calculations in a series of supercells, as shown in Table 3. When the supercell is enlarged from 221v1 to 222v1, we observe a relatively large drop in the Na<sup>+</sup> migration barrier. However, when the supercell size is further increased, the change in the Na<sup>+</sup> migration barrier is almost negligible, which justifies the use of the 222v1 supercell in previous studies.

Next, we investigate the relation between the diffusion coefficient and vacancy concentration. The theoretical model<sup>34</sup> based on an uncorrelated random walk predicts that

$$D = \omega c_v Z d^2 / 6 \quad (6)$$

where  $\omega$  is the jumping rate,  $c_v$  is the vacancy concentration,  $Z$  is the number of nearest Na<sup>+</sup> sites, and  $d$  is the distance between adjacent Na<sup>+</sup> sites. This equation implies that the diffusion coefficient is proportional to the vacancy concentration, provided that the interactions among Na ions can be neglected. When this condition is not satisfied (which is often the case in real systems), a common practice is to simply introduce a correlation factor  $f$ , and the proportionality between  $D$  and  $c_v$  is still assumed to hold ( $D = f\omega c_v Z d^2 / 6$ ), as we did in

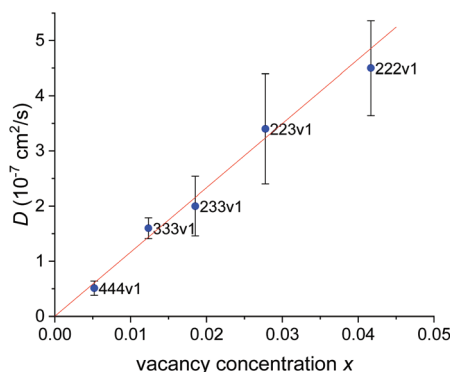


**Fig. 4** Diffusion coefficient ( $D$ ) vs. vacancy concentration ( $x$ ) calculated by DPMD simulations at  $T = 900$  K with different supercells. The blue points are data obtained from MD simulations; the red line is the least-square fit according to  $D = kx$ . The error bars are estimated from 10 slices each lasting 500 ps.

section 3.2. From our point of view, this assumption is somewhat arbitrary, as there is no guarantee that the correlation factor is independent of the vacancy concentration. To explicitly find out how the vacancy concentration affects the diffusion coefficient, we simulate Na<sup>+</sup> diffusion in 222v1, 223v1, 233v1, 333v1, and 444v1 supercells with the DP-G force-field, and calculate the diffusion coefficient in each supercell using eqn (2). On account of the increased computational cost, each simulation is shortened to 5 ns and cut into 10 slices for error estimation. As shown in Fig. 4, the diffusion coefficient does scale linearly with the vacancy concentration ( $r = 0.994$ ). This means that the correlation factor can be safely regarded as a constant under experimental conditions.

## 4. Conclusions

In this work, we have constructed a DP model to study Na<sup>+</sup> transport in Na<sub>3</sub>OBr. We found that the DP model can not only describe the migration process well, but also overcome the limitations imposed by the demanding computational cost of *ab initio* methods. In relatively simple tasks where *ab initio* calculations are affordable, such as the calculation of the NEB migration barrier on a 222v1 supercell and the determination of equilibrium lattice parameters at various temperatures, our DP model agrees well with *ab initio* methods, thus demonstrating its accuracy. Using the DP-based molecular dynamics technique, we have calculated the diffusion coefficient of Na<sub>3</sub>OBr in a temperature range of 700–1300 K and carried out an Arrhenius fit, which gives an activation energy of 0.42–0.43 eV. This is rather close to the NEB migration barrier (0.41–0.43 eV), suggesting that the finite temperature effect is negligible for Na<sub>3</sub>OBr. The extrapolated RT ionic conductivity at the experimental lattice parameter and vacancy concentration is estimated as  $1 \times 10^{-4}$ – $2 \times 10^{-4}$  mS cm<sup>-1</sup>, in the same order of magnitude as the experimental results. We have also investigated the influence of the vacancy concentration on the NEB migration barrier and diffusion coefficient, which reveals that the 222v1 supercell is large enough for the NEB migration barrier to converge, confirming the proportionality between the diffusion coefficient and vacancy concentration. This work has verified that the DP model works well for the theoretical simulation of sodium migration in Na<sub>3</sub>OBr, and one can anticipate further application of DP-based approaches to the exploration of new solid-state electrolytes with more desirable properties.

## Conflicts of interest

There are no conflicts to declare.

## Acknowledgements

We thank Dr Han Wang and Linfeng Zhang for the helpful discussion about the DeePMD method. This work is partly sup-

ported by the National Key Research and Development Program of China (No. 2016YFB0701100), the National Natural Science Foundation of China (Projects No. 21673005 and 21621061), and the High-performance Computing Platform of Peking University.

## References

- 1 H. Pan, Y.-S. Hu and L. Chen, Room-Temperature Stationary Sodium-Ion Batteries for Large-Scale Electric Energy Storage, *Energy Environ. Sci.*, 2013, **6**, 2338–2360.
- 2 Y. Lu, L. Li, Q. Zhang, Z. Niu and J. Chen, Electrolyte and Interface Engineering for Solid-State Sodium Batteries, *Joule*, 2018, **2**, 1747–1770.
- 3 T. Famprikis, P. Canepa, J. A. Dawson, M. S. Islam and C. Masquelier, Fundamentals of Inorganic Solid-State Electrolytes for Batteries, *Nat. Mater.*, 2019, **18**, 1278–1291.
- 4 S. Ohno, A. Banik, G. F. Dewald, M. A. Kraft, T. Krauskopf, N. Minafra, P. Till, M. Weiss and W. G. Zeier, Materials Design of Ionic Conductors for Solid State Batteries, *Prog. Energy*, 2020, **2**, 022001.
- 5 L. Zhang, K. Yang, J. Mi, L. Lu, L. Zhao, L. Wang, Y. Li and H. Zeng, Na<sub>3</sub>PSe<sub>4</sub>: A Novel Chalcogenide Solid Electrolyte with High Ionic Conductivity, *Adv. Energy Mater.*, 2015, **5**, 1501294.
- 6 O. Bohnke, S. Ronchetti and D. Mazza, Conductivity Measurements on Nasicon and Nasicon-Modified Materials, *Solid State Ionics*, 1999, **122**, 127–136.
- 7 S. Wenzel, T. Leichtweiss, D. A. Weber, J. Sann, W. G. Zeier and J. Janek, Interfacial Reactivity Benchmarking of the Sodium Ion Conductors Na<sub>3</sub>PS<sub>4</sub> and Sodium Beta-Alumina for Protected Sodium Metal Anodes and Sodium All-Solid-State Batteries, *ACS Appl. Mater. Interfaces*, 2016, **8**, 28216–28224.
- 8 Y. Zhao and L. L. Daemen, Superionic Conductivity in Lithium-Rich Anti-Perovskites, *J. Am. Chem. Soc.*, 2012, **134**, 15042–15047.
- 9 J. Zhu, Y. Wang, S. Li, J. W. Howard, J. Neufeind, Y. Ren, H. Wang, C. Liang, W. Yang, R. Zou, C. Jin and Y. Zhao, Sodium Ion Transport Mechanisms in Antiperovskite Electrolytes Na<sub>3</sub>OBr and Na<sub>4</sub>Oi<sub>2</sub>: An in Situ Neutron Diffraction Study, *Inorg. Chem.*, 2016, **55**, 5993–5998.
- 10 H. Fang and P. Jena, Sodium Superionic Conductors Based on Clusters, *ACS Appl. Mater. Interfaces*, 2019, **11**, 963–972.
- 11 Y. Wang, Q. Wang, Z. Liu, Z. Zhou, S. Li, J. Zhu, R. Zou, Y. Wang, J. Lin and Y. Zhao, Structural Manipulation Approaches Towards Enhanced Sodium Ionic Conductivity in Na-Rich Antiperovskites, *J. Power Sources*, 2015, **293**, 735–740.
- 12 Y. Sun, Y. Wang, X. Liang, Y. Xia, L. Peng, H. Jia, H. Li, L. Bai, J. Feng, H. Jiang and J. Xie, Rotational Cluster Anion Enabling Superionic Conductivity in Sodium-Rich Antiperovskite Na<sub>3</sub>O<sub>2</sub>Br<sub>4</sub>, *J. Am. Chem. Soc.*, 2019, **141**, 5640–5644.
- 13 J. Behler, Perspective: Machine Learning Potentials for Atomistic Simulations, *J. Chem. Phys.*, 2016, **145**, 170901.
- 14 H. Chan, B. Narayanan, M. J. Cherukara, F. G. Sen, K. Sasikumar, S. K. Gray, M. K. Y. Chan and S. K. R. S. Sankaranarayanan, Machine Learning Classical Interatomic Potentials for Molecular Dynamics from First-Principles Training Data, *J. Phys. Chem. C*, 2019, **123**, 6941–6957.
- 15 F. Noe, A. Tkatchenko, K.-R. Müller and C. Clementi, Machine Learning for Molecular Simulation, *Annu. Rev. Phys. Chem.*, 2020, **71**, 361–390.
- 16 L. Zhang, J. Han, H. Wang, R. Car and W. E, Deep Potential Molecular Dynamics: A Scalable Model with the Accuracy of Quantum Mechanics, *Phys. Rev. Lett.*, 2018, **120**, 143001.
- 17 L. Zhang, J. Han, H. Wang, W. A. Saidi, R. Car and W. E, End-to-End Symmetry Preserving Inter-Atomic Potential Energy Model for Finite and Extended Systems, *Adv. Neural Inform. Process. Syst.*, 2018, **31**, 4441–4445.
- 18 L. Zhang, D. Lin, H. Wang, R. Car and W. E, Active Learning of Uniformly Accurate Interatomic Potentials for Materials Simulation, *Phys. Rev. Mater.*, 2019, **3**, 023804.
- 19 K. Miwa and H. Ohno, Interatomic Potential Construction with Self-Learning and Adaptive Database, *Phys. Rev. Mater.*, 2017, **1**, 053801.
- 20 W. Li, Y. Ando, E. Minamitani and S. Watanabe, Study of Li Atom Diffusion in Amorphous Li<sub>3</sub>PO<sub>4</sub> with Neural Network Potential, *J. Chem. Phys.*, 2017, **147**, 214106.
- 21 K. Miwa and R. Asahi, Molecular Dynamics Simulations with Machine Learning Potential for Nb-Doped Lithium Garnet-Type Oxide Li<sub>7-x</sub>La<sub>3</sub>(Zr<sub>2-x</sub>Nb<sub>x</sub>)O<sub>12</sub>, *Phys. Rev. Mater.*, 2018, **2**, 105404.
- 22 A. Marcolongo, T. Binninger, F. Zipoli and T. Laino, Simulating Diffusion Properties of Solid-State Electrolytes Via a Neural Network Potential: Performance and Training Scheme, *ChemSystemsChem*, 2020, **2**, e1900031.
- 23 H. Wang, L. Zhang, J. Han and W. E, Deepmd-Kit: A Deep Learning Package for Many-Body Potential Energy Representation and Molecular Dynamics, *Comput. Phys. Commun.*, 2018, **228**, 178–184.
- 24 G. Kresse and J. Furthmüller, Efficient Iterative Schemes for Ab Initio Total-Energy Calculations Using a Plane-Wave Basis Set, *Phys. Rev. B: Condens. Matter Mater. Phys.*, 1996, **54**, 11169–11186.
- 25 G. Kresse and D. Joubert, From Ultrasoft Pseudopotentials to the Projector Augmented-Wave Method, *Phys. Rev. B: Condens. Matter Mater. Phys.*, 1999, **59**, 1758–1775.
- 26 J. P. Perdew, A. Ruzsinszky, G. I. Csonka, O. A. Vydrov, G. E. Scuseria, A. C. Lucian, X. Zhou and K. Burke, Restoring the Density-Gradient Expansion for Exchange in Solids and Surfaces, *Phys. Rev. Lett.*, 2008, **100**, 136406.
- 27 H. Jiang, Structural and Electronic Properties of Zr<sub>x</sub>Sn<sub>2</sub> and Hf<sub>x</sub>Sn<sub>2</sub> (X = S and Se) from First Principles Calculations, *J. Chem. Phys.*, 2011, **134**, 204705.
- 28 F. Tran, J. Stelzl and P. Blaha, Rungs 1 to 4 of Dft Jacob's Ladder: Extensive Test on the Lattice Constant, Bulk Modulus, and Cohesive Energy of Solids, *J. Chem. Phys.*, 2016, **144**, 204120.

- 29 Y. Zhang, H. Wang, W. Chen, J. Zeng, L. Zhang, H. Wang and W. E, Dp-Gen: A Concurrent Learning Platform for the Generation of Reliable Deep Learning Based Potential Energy Models, *Comput. Phys. Commun.*, 2020, **253**, 107206.
- 30 S. Plimpton, Fast Parallel Algorithms for Short-Range Molecular-Dynamics, *J. Comput. Phys.*, 1995, **117**, 1–19.
- 31 G. Kresse, M. Marsman and J. Furthmüller, *Vasp the Guide*, Universität Wien, Vienna, 2016.
- 32 H. Fang, S. Wang, J. Liu, Q. Sun and P. Jena, Superhalogen-Based Lithium Superionic Conductors, *J. Mater. Chem. A*, 2017, **5**, 13373–13381.
- 33 Y. Zhang, Y. Zhao and C. Chen, Ab Initio Study of the Stabilities of and Mechanism of Superionic Transport in Lithium-Rich Antiperovskites, *Phys. Rev. B: Condens. Matter Mater. Phys.*, 2013, **87**, 134303.
- 34 H. Meherer, *Diffusion in Solids*, Springer, Berlin, 2007.
- 35 G. Henkelman and H. Jonsson, Improved Tangent Estimate in the Nudged Elastic Band Method for Finding Minimum Energy Paths and Saddle Points, *J. Chem. Phys.*, 2000, **113**, 9978–9985.
- 36 G. Henkelman, B. P. Uberuaga and H. Jonsson, A Climbing Image Nudged Elastic Band Method for Finding Saddle Points and Minimum Energy Paths, *J. Chem. Phys.*, 2000, **113**, 9901–9904.
- 37 Transition State Tools for Vasp, <http://theory.cm.utexas.edu/vtsstools/index.html>.
- 38 A. H. Larsen, J. J. Mortensen, J. Blomqvist, I. E. Castelli, R. Christensen, M. Dulak, J. Friis, M. N. Groves, B. Hammer, C. Hargus, E. D. Hermes, P. C. Jennings, P. B. Jensen, J. Kermode, J. R. Kitchin, E. L. Kolsbjerg, J. Kubal, K. Kaasbjerg, S. Lysgaard, J. B. Maronsson, T. Maxson, T. Olsen, L. Pastewka, A. Peterson, C. Rostgaard, J. Schiotz, O. Schutt, M. Strange, K. S. Thygesen, T. Vegge, L. Vilhelmsen, M. Walter, Z. H. Zeng and K. W. Jacobsen, The Atomic Simulation Environment—a Python Library for Working with Atoms, *J. Phys.: Condens. Matter*, 2017, **29**, 273002.
- 39 J. A. Dawson, P. Canepa, T. Famprikis, C. Masquelier and M. S. Islam, Atomic-Scale Influence of Grain Boundaries on Li-Ion Conduction in Solid Electrolytes for All-Solid-State Batteries, *J. Am. Chem. Soc.*, 2018, **140**, 362–368.